Crystal growth, Yb^{3+} spectroscopy, concentration quenching analysis and potentiality of laser emission in Ca$_{1-x}$Yb$_x$F$_{2+x}$

Crystal growth, Yb^{3+} spectroscopy, concentration quenching analysis and potentiality of laser emission in Ca$_{1-X}$Yb$_X$F$_{2+X}$

Masahiko Ito[1,3]**, Christelle Goutaudier**[1]**, Yannick Guyot**[1]**, Kheirreddine Lebbou**[1]**, Tsuguo Fukuda**[2] **and Georges Boulon**[1]

[1] Physical Chemistry of Luminescent Materials, Claude Bernard/Lyon 1 University, UMR 5620 CNRS, Bâtiment A Kastler, 10 rue Ampère, 69622 Villeurbanne Cedex, France
[2] Institute of Multidisciplinary Research for Advanced Materials, Tohoku University, 2-1-1 Katahira, Aoba-ku, Sendai 980-8577, Japan

E-mail: ito@pcml.univ-lyon1.fr

Abstract

Ca$_{1-X}$Yb$_X$F$_{2+X}$ crystals were grown by two different methods: simple melting under CF$_4$ atmosphere and the laser heated pedestal growth (LHPG) method under Ar atmosphere. Spectroscopic characterization (absorption, emission, Raman spectroscopy and decay curves) was carried out to identify Stark levels of Yb^{3+} transitions in the different crystallographic sites of the cubic structure in Ca$_{1-X}$Yb$_X$F$_{2+X}$ crystals. The Yb^{3+} concentration dependence of the experimental decay time was analysed by using concentration gradient fibre in order to understand involved concentration quenching mechanisms. Under Yb^{3+} ion infrared pumping, self-trapping and up-conversion non-radiative energy transfer to unexpected rare earth impurities (Er^{3+}, Tm^{3+}) has been observed in the visible region and interpreted by a limited diffusion process within the Yb^{3+} doping ion subsystem towards impurities. The main parameters useful for a theoretical approach of laser potentiality have been given as $\tau_{\text{rad}} = 2.05$ ms, $N_0 = 7.47 \times 10^{21}$ cm^{-3} (32 mol%) and $N_{\text{m}} = 6.39 \times 10^{21}$ cm^{-3} (26.5 mol%).

1. Introduction

Yb^{3+} is the most promising ion that can be used in a non-Nd^{3+} laser in the near-IR spectral range of 1030 nm, which is roughly in the same range as Nd^{3+} emission wavelength, under laser diode pumping with a smaller quantum defect than in Nd^{3+}-doped crystals (10% instead of 25%). The Yb^{3+} ion has several advantages compared with Nd^{3+} due to its very simple

[3] Author to whom any correspondence should be addressed.

energy level scheme, being composed of only two levels. This makes it possible to avoid up-conversion, excited state absorption and concentration quenching within a large concentration domain. Up to now, several oxides have been thoroughly investigated, and the spectroscopic properties of Yb^{3+}-doped host materials are leading to general methods of evaluation [1–3]. Our main objective is now to make a contribution for Yb^{3+}-doped fluorides. Among such hosts, we are dealing with the main families of laser crystals such as CaF_2, $LiYF_4$, $LiLuF_4$, BaY_2F_8 and KY_3F_{10}. In the present paper we focus our scientific programme on a Yb^{3+}-doped CaF_2 fluoride cubic host. Such un-doped crystals are now being grown with large diameter, mainly to be used as window materials for excimer lasers which are needed in semiconductor technology as optical lithography. We think that the growth of high quality CaF_2 single crystals, which are characterized by a high value of thermal conductivity (10 W m^{-1} K^{-1}), much higher than other fluoride laser crystals (5 W m^{-1} K^{-1} in $LiYF_4$) and as high as YAG (10.7 W m^{-1} K^{-1}), should also contribute to the development of rare earth-doped fluoride laser single crystals. In this paper, on the one hand we are investigating basic research based on the detailed spectroscopy of $Ca_{1-X}Yb_XF_{2+X}$ crystals which are grown by two different methods and, on the other hand, we are analysing quenching mechanisms which should be useful for estimating their potential development as optical materials, mainly as tuneable solid state lasers due to their room-temperature broad band emission.

2. Structure and nature of crystallographic sites

CaF_2 is the typical fluorite-type crystal. It is known to form a $Ca_{1-X}RE_XF_{2+X}$ type solid solution with trivalent rare-earth fluorides of up to nearly 40 mol% dopant concentration [4]. The structure of CaF_2 can be regarded as a simple cubic array of touching F^- ions with every second void occupied by a Ca^{2+} ion. When a Ca^{2+} ion is substituted by trivalent rare earth, charge balance compensating F^- ions should enter the fluorite structure. Up to now many structural investigations have been carried out on $Ca_{1-X}RE_XF_{2+X}$ type materials [5–10] leading to dominant defect structures. At low concentration (dopant concentrations of less than 1 mol%) the additional F^- ion goes into a next-nearest-neighbour void of the trivalent rare earth ion giving isolated tetragonal (C_{4V}), trigonal (C_{3V}) or rhombic (C_{2V}) defects. These isolated defects have already been well studied by electron paramagnetic resonance and optical spectroscopy [5, 11–13]. However, for dopant concentration greater than 0.1 mol%, anion clusters involving more than one dopant cation are formed [5]. These clusters have been studied by x-ray diffraction, EXAFS (extended x-ray absorption fine structure) and neutron diffraction [5–10]. Two kinds of anion cluster, which associate anionic vacancies on the normal F^- ion site and interstitial anions in two different sites: F' ($1/2, x, x; x \approx 0.37$) and F'' ($x, x, x; x \approx 0.41$), have been described depending on the size and the coordination of the dopant cations. When the dopant size is large, when nine- or ten-fold coordination is geometrically possible, small 1:0:3 anion clusters (1 anionic vacancy, 0 F' and 3 F'' interstitial anions) are the most stable defects. It can be regarded as a deformed dimer. On the other hand, when dopant cation size is small, eight-fold coordination is favoured and large 8:12:1 cuboctahedral anion clusters are formed [5, 7, 8]. This 8:12:1 cuboctahedral anion clusters can also represent M_6F_{37} (M = cation) clusters [9, 10], which are composed of six corner-sharing MF_8 square-antiprisms enclosing a cuboctahedron of anions which contains an additional anion at its centre. The analagous un-doped fluorite consists of six edge-sharing MF_8 cubes enclosing a cube of anions (M_6F_{32}), so the formation of the M_6F_{37} clusters involves incorporation of additional anions, which can be represented as $M_6F_{32} + 5F \rightarrow M_6F_{37}$. The schema of both, the M_6F_{37} cluster and the un-doped fluorite analogue, M_6F_{32}, are shown in figure 1. This M_6F_{37} anion cluster formation can be recognized by considering the well known fluorite-type superstructures
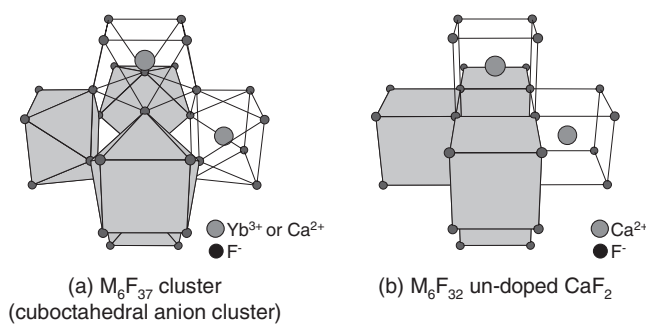
(a) M_6F_{37} cluster
(cuboctahedral anion cluster)

(b) M_6F_{32} un-doped CaF_2

Figure 1. Schema of (a) a M_6F_{37} cluster in $Ca_{1-X}RE_XF_{2+X}$ crystals and (b) its un-doped fluorite analogue, M_6F_{32}.

such as KY_3F_{10} [14] and $Na_7Zr_6F_{31}$ [15]. Indeed, there may be even more structures which can be described by a basic building block, M_3F_{21}, consisting of a triangular group of three square-antiprism sharing corners around a three-fold axis, i.e. half of the M_6F_{37} cluster. These clusters link together in various ways to form various structures. The cuboctahedral anion cluster structures are in fact a subset of them [9].

From the structural studies above, we considered the crystallographic sites of Yb^{3+}-doped fluorite ($Ca_{1-X}Yb_XF_{2+X}$). Since Yb^{3+} has a small cationic radius among rare-earth ions, it should favour keeping eight-fold coordination. The isolated tetragonal, trigonal or rhombic defects require uncomfortable nine-fold coordination, therefore it could not be the principal site. Even though it could exist, we found it only for low concentration where the formation of anion clusters involving more than one ytterbium is rather difficult. Also because of the coordination number, dimer (i.e. 1:0:3 anion clusters) formation is uncomfortable. The square-antiprism sites in cuboctahedral anion clusters should be the principal sites in the Yb^{3+} concentration we are studying. Probably, for low concentration, M_3F_{21} clusters are first formed and successive various cuboctahedral-related clusters are formed with the increase of concentration. However, there are a huge number of structural possibilities and each cuboctahedral-related cluster should have similar structure, hence its spectroscopic properties become an average of them. Then, it is hardly possible to separate them and to assign them exactly due to the spreading of the optical spectra, as for the disordered crystals.

3. Crystal growth

$Ca_{1-X}Yb_XF_{2+X}$ crystals were prepared by two different methods as described below. It is important to compare the spectroscopic properties on the growth conditions because some properties may change depending on the crystal quality which was influenced by growth conditions.

3.1. Synthesis of crystalline samples by simple melting at the Tohoku University (Sendai)

The main objective of this synthesis was to provide seed crystals and feed rods for the laser heated pedestal growth (LHPG) technique to grow single crystalline fibres as described in the next section.

$Ca_{1-X}Yb_XF_{2+X}$ ($X = 0.005, 0.02, 0.05, 0.15$ and 0.3) crystals were prepared by simply melting mixtures of commercially available powders of CaF_2 and YbF_3 with the purity of 4N. The furnace was driven with a 30 kW RF generator and a carbon crucible was used for melting
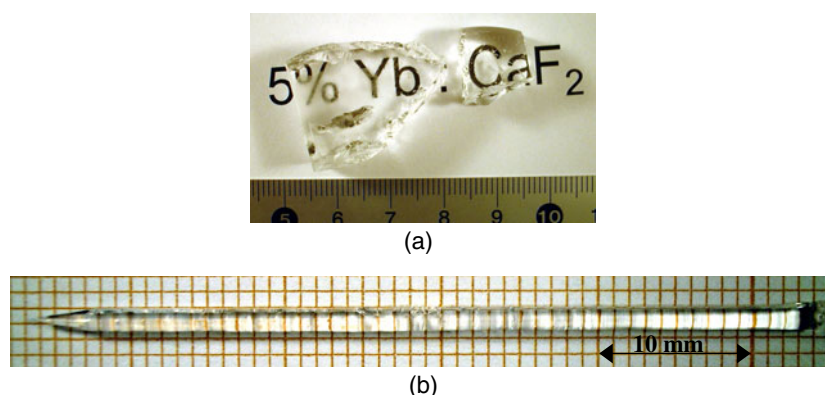
Figure 2. (a) Some pieces of $Ca_{0.95}Yb_{0.05}F_{2.05}$ crystal prepared by simple melting and (b) a $Ca_{1-X}Yb_XF_{2+X}$ ($X = 0$–0.15) concentration gradient fibre grown by the LHPG method.

(This figure is in colour only in the electronic version)

materials. The furnace was vacuumed up to 10^{-4} Torr prior to synthesis to eliminate oxygen and/or water, and then CF_4 gas was slowly introduced. The melting was performed under CF_4 atmosphere. After completely melting materials, the furnace was slowly cooled down to room temperature.

Large crystalline ingots could be prepared very rapidly and efficiently by this method. Now, un-doped CaF_2 crystals of few inches diameter are industrially grown, but not high concentration trivalent rare earth-doped crystals. The growth of trivalent rare earth-doped crystals turns out to be difficult due to the occurrence of supercooling phenomena. Nevertheless, this method allowed us to prepare these crystals of a few centimetres in size in only a few hours. Figure 2(a) shows some pieces of un-polished $Ca_{9.95}Yb_{0.05}F_{2.05}$ rough crystals to show the size of the pieces. Although the ingots are in fact disordered samples composed of some large single crystals, each part of ingot has as good transparency as a single crystal one. As the first objective of this synthesis, we could provide this ingot for seed crystals and feed rods for the LHPG method as described in the next section. Moreover, it is worthwhile studying the spectroscopic characterizations of such Yb^{3+}-doped samples to compare them with fibre samples grown by the LHPG technique.

All the $Ca_{1-X}Yb_XF_{2+X}$ crystals grown by this method were estimated to have a cubic fluorite-type structure by powder x-ray diffraction. The lattice constant became larger in proportion to the concentration of dopant, even though the Yb^{3+} ion ($r = 0.985$ Å) has a smaller ionic radius than the Ca^{2+} ion ($r = 1.12$ Å). This dependence came from the existence of interstitial fluorine ions as discussed in [4]. The linear relationship between the lattice constant in ångström units and the concentration of Yb^{3+} ions is given by the following equation (1):

$$a = a_0 + 0.109X. \tag{1}$$

Here, a_0 is the lattice constant of the un-doped crystal.

3.2. Crystal growth by the LHPG method at the UCBLyon1

The LHPG method is one of the suitable methods for evaluating crystals as laser materials since it needs only a small amount of raw materials and the growth rate is much faster than other
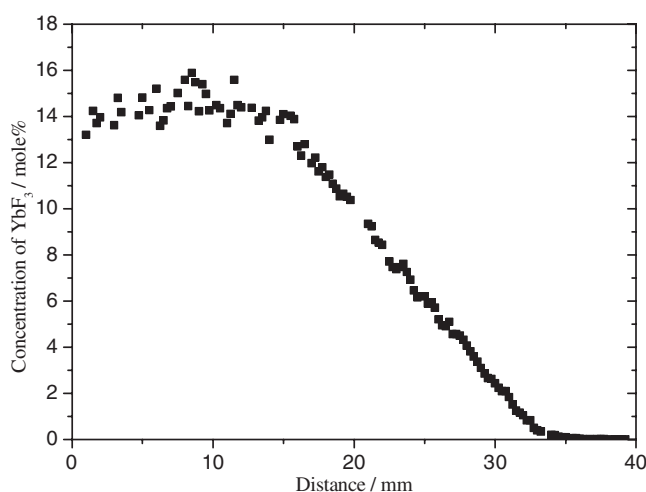
Figure 3. Evaluation of the Yb^{3+} concentration along the fibre positions, investigated using an electron probe microanalyser.

methods such as the Czochralski method. In addition, we have recently grown concentration gradient fibres by this method [16, 17]. Using the special ceramic rod, which is composed of two different dopant concentrations and cut along a slant direction, it is possible to prepare original single-crystalline samples with variable concentrations of dopant in an extremely wide range. Such fibres are very useful for spectroscopic characterizations, as shown recently [1, 16, 17].

The LHPG method was applied to prepare $Ca_{1-X}Yb_XF_{2+X}$ mono-doped crystals ($X = 0.005, 0.02, 0.05, 0.15$ and 0.3) and concentration gradient fibres ($X = 0–0.15$ and $0.05–0.3$). As already mentioned, the feed rods and the seed crystals were prepared from simple melting ingots. The furnace was vacuumed up to 10^{-4} Torr and subsequently pure Ar gas was slowly introduced. This atmosphere treatment was performed twice prior to synthesis. The growth was performed under Ar atmosphere. The growth rate and the feed rod supply rate were 30 and 20 mm h^{-1}, respectively. The fibres were steadily grown, though slight evaporation of CaF_2 was observed during the growth. Figure 2(b) shows $Ca_{1-X}Yb_XF_{2+X}$ (X varied from 0 to 0.15) concentration gradient fibres grown by the LHPG method. As can be seen, transparent crystalline fibres with diameter about 1.0 mm were obtained. Any inclusions were not seen in as-grown crystalline fibres. The surface of fibres was smooth. Electron probe microanalysis proved that the ytterbium concentration gradually changed along the fibre position (figure 3).

4. Procedure of the spectroscopic characterization

Absorption spectra were measured with a Lambda 900 spectrophotometer equipped with a continuous flow helium refrigerator. Emission spectra were acquired by exciting the samples with a QUANTEL Nd^{3+}:YAG pumped dye laser using a mix of LD700 and DCM dye. The dye laser light was converted to the 930–980 nm region by way of a H$_2$ Raman shift cell. The laser beam spot was about 500 μm in size and the energy was about 0.8 mJ. The infra-red emission was detected in a perpendicular direction to the excited beam with a Jobin–Yvon HRS1 monochromator equipped with a 1000 nm blazed grating, with a cooled Ge-detector, and the signal was processed with a STANDFORDS boxcar SRS 250. A closed circuit helium refrigeration system (SMC, TBT air–liquid) was used for the low temperature (12 K) measurements. The visible emission was detected by a ORIEL spectrometer coupled with a
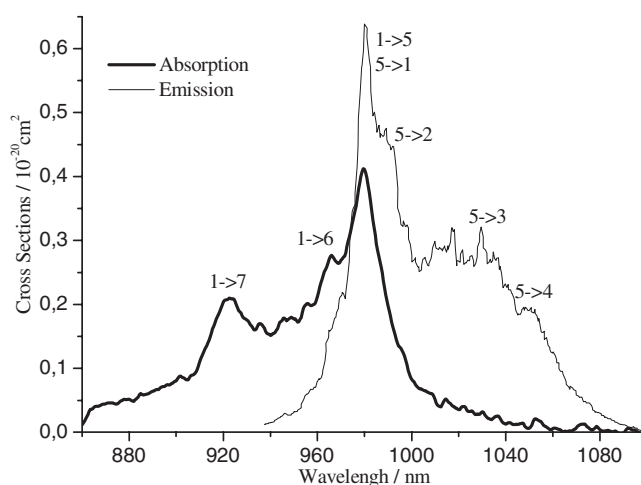
Figure 4. The room temperature absorption and emission (under $\lambda_{exc} = 930$ nm) spectra of $Ca_{0.995}Yb_{0.005}F_{2.005}$ crystal by simple melting.

gated intensified CCD camera (ANDOR/ORIEL INTASPEC V ICCD). The decay curves were recorded with a Lecroy LT 342 digital oscilloscope. The Raman spectrum was measured by a Dylor XY triple spectrometer using the 514.5 nm line of an ionized argon laser.

5. Results and discussion

5.1. Assignment of absorption and emission transitions of Yb^{3+} multisites and excited state dynamics

The room temperature absorption and emission spectra of $Ca_{0.995}Yb_{0.005}F_{2.005}$ crystals, which were prepared by simple melting, are shown in figure 4. We have chosen one sample doped by the lowest (0.5 mol%) concentration of Yb^{3+} ions to avoid the cross-section calculation errors caused by a re-absorption effect mainly of resonant transitions. The emission cross-section value was calculated using the Füchtbauer–Ladenburg equation [18]. The $^2F_{7/2} \leftrightarrow {}^2F_{5/2}$ lowest energy resonant transition line was located at 980 nm. One can recognize here, that the cross-section value of this 0-phonon line is different between absorption and emission spectra. This is due to the energy migration from several cationic centres to the lowest energy centre, which is mentioned later in figure 6. Other transitions between Stark levels were located from 920 to 1060 nm. The shapes of absorption and emission spectra are quite broad. These shapes can be connected to the appearance of several crystallographic sites in the CaF_2 structure and the thermal spreading of these spectra. Such broad band spectra are similar to those of disordered materials such as glasses and then expected to be used for tuneable solid state laser sources. The stimulated emission cross-section around 1030 nm was estimated to be 3.0×10^{-21} cm^2, which is not high when we compare it with Yb^{3+}:YAG (around 2.0×10^{-20} cm^2 [17]) but it is a reasonable value compared with other fluoride hosts (for example around 0.3×10^{-20} and 1.0×10^{-20} cm^2 for Yb^{3+}:LiYF$_4$ in σ and π polarization respectively [19]).

Low temperature measurements at 12 K were carried out to avoid broadening of spectra and determine the exact Stark level positions. The emission spectra were looking quite similar whatever the nature of the crystal growth technique. As an example, figure 5 shows absorption and emission spectra of $Ca_{0.995}Yb_{0.005}F_{2.005}$ crystal prepared (a) by the simple melting method

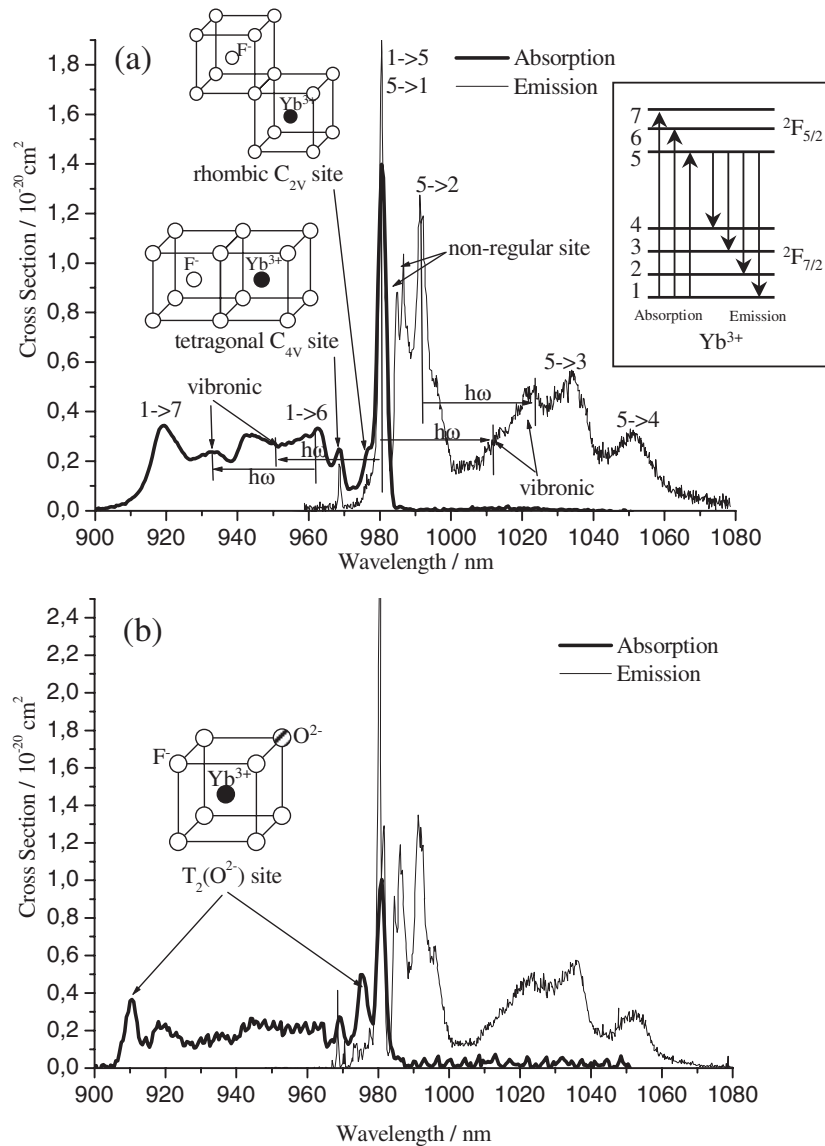**Figure 5.** Absorption and emission (under $\lambda_{\text{exc}} = 930$ nm) spectra of Ca$_{0.995}$Yb$_{0.005}$F$_{2.005}$ crystal at low temperature ($T = 12$ K) prepared (a) by simple melting and (b) by the LHPG method. The arrows indicate the expected vibronic lines shifted from the electronic line of the phonon energy $\hbar\omega = 321$ cm^{-1}.

and (b) by the LHPG method. The assignment of Yb^{3+} Stark levels is known to have problems since the appearance of a strong electron–phonon coupling mixes both electronic and vibronic transitions of the main site. In the case of the Yb^{3+} ion occupying several cationic sites, the spectra are becoming obviously further complex. Figure 5 shows clearly different types of sites, and electronic and vibronic transitions.

Previous research [12, 13, 20, 21] helped us to assign the $1 \leftrightarrow 5$ resonant transition of the tetragonal C$_{4V}$ site at 968.5 nm, the rhombic C$_{2V}$ site at 977 nm and also the T$_2$(O^{2-}) site, with
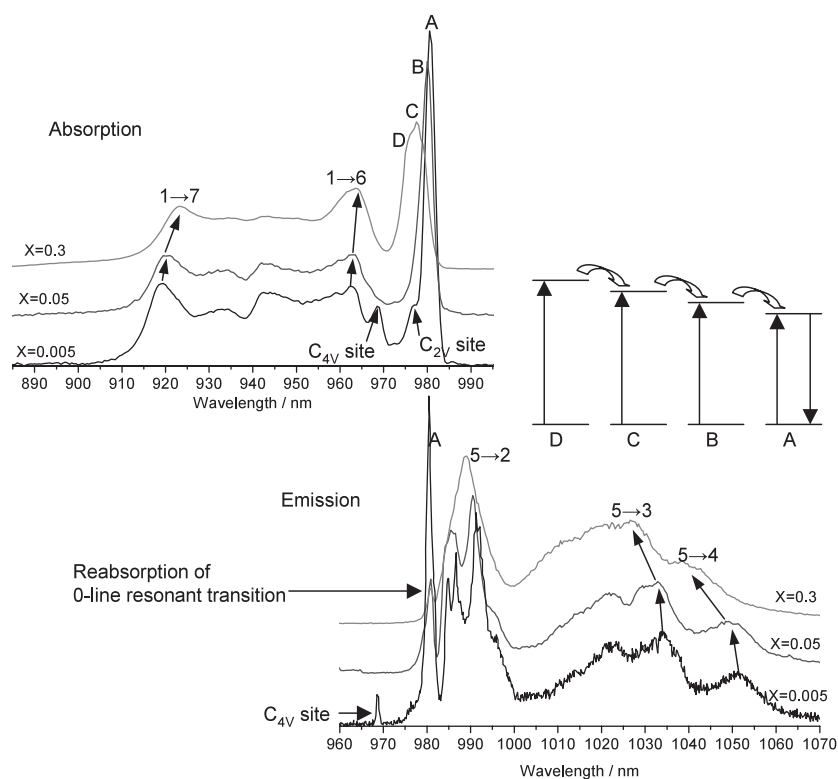
Figure 6. The low temperature ($T = 12$ K) absorption and emission ($\lambda_{exc} = 930$ nm) spectra of $Ca_{1-X}Yb_XF_{2+X}$ crystal ($X = 0.005$, 0.05 and 0.3) by simple melting.

the presence of one O^{2-} anion in substitution for one F^- anion in the corner of the anion cube at 975 and 910.5 nm. These isolated tetragonal C_{4V} and rhombic C_{2V} defect sites were observed only for the lowest (0.5 mol%) concentration. According to structural studies (section 2), these defects require the geometrically uncomfortable nine-fold coordination, hence they exist only where the formation of the anion cluster involving more than one ytterbium is rather difficult. $T_2(O^{2-})$ sites were observed only in the crystals grown by the LHPG method. This could be explained by the fact that under the LHPG conditions using pure argon atmosphere, ppm order of oxygen ions always existed and they could react with fluorides during crystal growth, whereas a CF_4 atmosphere for simple melting is known to react with oxygen and effectively eliminate it. The cubic O_h site with $1 \leftrightarrow 5$ resonant transition lines located at 963 nm, [12, 13, 20], were not detected in our samples. Such cubic site observation needs to work on very low concentration (less than 0.2 at.%) since charge compensating F^- ions must be situated somewhere far from the Yb^{3+} site in such a case. Our concentrations are much higher and we were not able to see any cubic sites in samples of concentrations from 0.5 to 30 mol%.

The other main lines seen in both absorption and emission spectra should be assigned to the principal Yb^{3+} site that is the set of square-antiprism sites. The electronic absorption transitions ($1 \to 5$, $1 \to 6$, $1 \to 7$) and the resonant $5 \to 1$ and non-resonant ($5 \to 2$, $5 \to 3$, $5 \to 4$) electronic emission transitions are observed. In addition, vibronic lines can be also seen. One of the main difficulties of assignment is to separate such electronic and vibronic lines. To identify a vibronic peak, Buchanan *et al* [22] have already proposed the comparison between absorption and emission symmetric spectra around the 0-phonon line. This method is

Table 1. Experimental decay times for each wavelength at 12 K. The main transitions belong to the square-antiprism sites in the cuboctahedral clusters.

Wavelength (nm)	968.5	980.5	985	987	991.5	1024	1034.5	1051.5
Decay time (ms)	2.21	1.97	2.06	2.05	1.95	1.95	1.96	1.97
Estimation of sites	Tetragonal	$5 \rightarrow 1$	?	?	$5 \rightarrow 2$	Vibronic	$5 \rightarrow 3$	$5 \rightarrow 4$

however difficult to apply in the case of crystals accepting multisites because the broad peaks make it difficult to identify the coincidence of peaks with the existence of several sites. Our own experimental approach has used absorption, emission spectra and Raman spectra.

Firstly, vibronic transitions were assigned with the help of the Raman spectrum. The Raman spectrum has a very simple structure: only one sharp peak situated at 321 cm^{-1} in the lowest doped sample. This unique peak becomes slightly broader in the 30% doped sample. Other local modes which are related to clusters may exist in high-doped samples, but we could not find any additional peaks. Thus, we have only considered the 321 cm^{-1} line for vibronic transition assignments. Due to the electron–phonon coupling, the vibronic lines should be found at the frequency of 321 cm^{-1} from the different 0-phonon electronic transitions. Some pairs of signals were found to stay in this frequency as can be seen in figure 5. The 1012 nm line could be assigned as the vibronic transition from the $5 \rightarrow 1$ resonant transition line. The symmetric of the 1012 nm line is 950 nm, this position is obscure in the broad absorption. Nevertheless, we have estimated there is a vibronic transition, which is difficult to resolve due to the overlapping between the 962.5 and 942.5 nm lines. The 1024 nm line could also be assigned as the vibronic overtone line of the 991.5 nm line. Consequently, the 991.5 nm line could be an electronic transition which has been assigned as the $5 \rightarrow 2$ transition. In a similar approach, the 933.5 nm line could be the vibronic line of the $1 \rightarrow 6$ (962.5 nm) transition.

Secondly, experimental decay times for each wavelength were measured to confirm the selection of different crystallographic sites. Table 1 shows exponential decay time values for different wavelengths. The majority include decay times around 1.95–1.97 ms from the same energy level of the square-antiprism site, whereas the 968.5, 985 and 987 nm lines have longer decay times, and therefore could be separated as different transition sites. The small peak at 968.5 nm had already been assigned as the resonant transition of the tetragonal C_{4V} site. The 985 and 987 nm lines were observed even for high concentration, therefore we cannot interpret them like low concentration sites such as tetragonal sites. We estimated they should be emission transitions from the non-regular square-antiprism sites. The absorption at 942.5 nm could not be assigned by the methods above. We have admitted this absorption was vibronic, but further study is needed to clarify it. In such a case, infrared absorption spectroscopy should be useful, but here our attempts were unsuccessful.

Above 0.5 mol%, we can start to speak in terms of a growing number of square-antiprism sites in the form of cuboctahedral anion clusters. Clusters involving more than one cation appear in the literature above 0.1 mol% [5]. The existence of clusters containing more and more Yb^{3+} ions from 0.5 to 30 mol% in our samples is characterized by a $1 \rightarrow 5$ absorption electronic transition at 980.5 nm slightly shifted to shorter wavelengths, as can be seen in figure 6. It is possible to mention at least four types of site: A, B, C and D, with an interesting observation of the lowering of the crystal field from low to high concentrations. In this figure 6, the reduction of the crystal field splitting of each $^2F_{5/2}$ and $^2F_{7/2}$ manifold is clearly seen: $1 \rightarrow 7$ is shifted to longer wavelengths (919 $\rightarrow$ 923 nm) and $5 \rightarrow 4$ shifted to shorter wavelengths (1051.5 $\rightarrow$ 1041 nm). This reduction of the crystal field splitting is explained by the extension of the lattice constant in proportion to the concentration of dopant which has been observed in our samples in agreement with previous results [4]. Moreover, another

Table 2. Energy level splitting of square-antiprism sites in $Ca_{1-X}Yb_XF_{2+X}$ crystals.

		Energy (cm^{-1})		
Yb^{3+} concentration		0.5 mole%	5 mole%	30 mole%
$^2F_{5/2}$	7	10 881	10 870	10 834
	6	10 390	10 384	10 379
	5	10 199 (A)	10 204 (B)	10 230 (C)
				10 246 (D)
$^2F_{7/2}$	4	689	675	593
	3	532	518	462
	2	113	103	88
	1	0	0	0

remarkable observation has to be mentioned in the spectral domain of the 1 ↔ 5 0-phonon line: absorption and emission lines do not overlap for each concentration as expected. Whereas absorption lines are shifted to higher energies (from A to D), emission lines are roughly located at the same wavelength (line A) near 980.5 nm independently of the Yb^{3+} concentration. It means that the main emitting centre is always the same (line A), seen at both low and high concentrations. As a consequence, there is a strong diffusion process among the different clusters before reaching the emitting ion (see inset in figure 6). We can recognize that this is one reason why the calculated emission cross-section value of the 1 ↔ 5 resonant transition line (line A at 980.5 nm) showed a higher value than that of the absorption cross-section value as can be already seen in figures 4 and 5.

We can also see in figure 6 the occurrence of the strong re-absorption phenomenon of the emission resonant transition (line A), typically by a self-trapping process as has already been observed and interpreted in almost all Yb^{3+}-doped crystals: sesquioxides [17, 23, 24], YAG [25]. This phenomenon was also easily observed at room-temperature measurements.

Finally, the Stark levels of the main site, which should indeed be a set of several square-antiprism sites, are defined in table 2.

5.2. Attempt at verification by the barycentre law

Consequently, to verify our interpretation of Yb^{3+} energy levels in CaF_2, we have then applied the barycentre plot method, introduced by Antic-Fidancev [26], based on the fact that the spin–orbit splitting between $^2F_{7/2}$ and $^2F_{5/2}$ is host independent, and equal to the free-ion energy separation. For rare earth ions, it was shown that the $^{2S+1}L_J$ level barycentre as a function of any other barycentre of isolated level in the $4f^n$ ground configuration, exhibits a linear dependence within the experimental errors. Especially for Yb^{3+}-doped crystals, when taking the lowest Stark level as the origin of energy and plotting the $^2F_{5/2}$ manifold energy barycentre versus the $^2F_{7/2}$ one, the representative points generally describe a straight line characterized by a slope of unity. In the case of ytterbium, the energy separation between the two manifolds is about 10 200 cm^{-1}. We can neglect the J-mixing to a good approximation and consider constant this energy whatever the host. The $^2F_{5/2}$ level barycentre as a function of the $^2F_{7/2}$ level barycentre for several hosts is presented in figure 7. According to the assignment of Stark levels of Yb^{3+}:CaF_2, we have placed 0.5%, 5% and 30% samples on the barycentre plot to confirm the accuracy of our results as already discussed in YAG [25] and LiYF₄ [19]. Stark levels for $Ca_{1-X}Yb_XF_{2+X}$ crystals are pretty well positioned on the theoretical slope for the three concentrations.
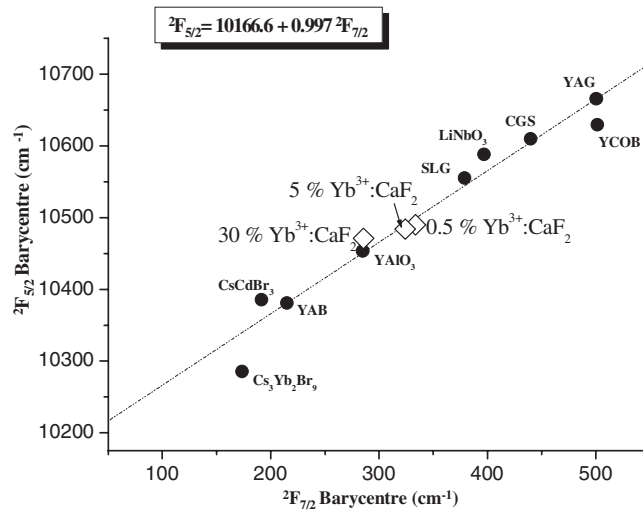
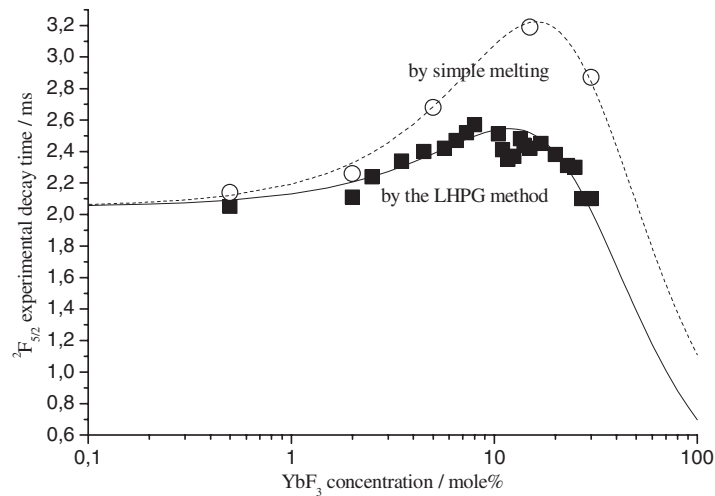**Figure 7.** Barycentre plot for various Yb^{3+}-doped host materials.

Figure 8. $^2F_{5/2}$ experimental decay time dependence on dopant concentration at room temperature. $\lambda_{exc} = 930$ nm and $\lambda_{measure} = 990$ nm. Broken and continuous curves indicate theoretical fitting by equation (5).

5.3. Concentration quenching study

Identifying the origin of the concentration dependence of the observed experimental decay time allows understanding of excited state dynamics. Such mechanisms have been recently studied in sesquioxides [1, 17, 23, 24] and YAG [25]. Figure 8 shows $^2F_{5/2}$ experimental decay time dependence on Yb^{3+} concentration in CaF_2. The white circles show decay times of the samples by simple melting and the black squares show decay times of the samples by the LHPG method. We found that decay profiles had exponential behaviour on two orders of magnitude at all concentrations. The concentration dependence of decay times can be generally divided into two regimes as can be seen in figure 8:

(i) The lower concentration range, up to 12 mol% for the LHPG method and 16 mol% for the simple melting method in which the experimental decay time increases. This is due to the self-trapping or the radiative energy transfer between Yb^{3+} neighbour ions by $^2F_{7/2} \leftrightarrow {}^2F_{5/2}$ resonant transition. We mention here that decay times of the LHPG fibres were recorded along the growth axis of the fibre just by translating it vertically to the exciting beam, i.e. the fibre was homogeneously excited for all concentrations. Because the volume of materials excited is steady, the self-trapping due to the geometrical effect can be supposed to be a constant value for each concentration.

(ii) The higher concentration range, in which the experimental decay time decreases when the doping rate increases up to 30 mol% (7.2×10^{21} at. cm^{-3}). This is related to the self-quenching effect.

Due to the presence of the multisite nature of the samples as mentioned in section 2, it is again difficult to only measure the decay time of one type of site. However, by monitoring, at room temperature, the $5 \rightarrow 2$ non-resonant transition emission around 990 nm, we have averaged the decay time of the main site appearing at each concentration.

5.3.1. First regime: self-trapping effect. Decay time measurement is known to be perturbed by experimental configuration. However, as already mentioned above, all measurements have been performed in the same configuration and the LHPG fibre was homogeneously excited for all concentrations. Thus, self-trapping due to the geometrical effect can be supposed to be a constant value for each concentration. As a consequence, only concentration dependence could be treated in figure 8.

When we considered figure 8 in relation to growth methods, we recognized easily the differences in the decay time dependence on dopant concentration between the two different growth methods. Namely the LHPG crystals showed lower decay time variation than that of the simple melting samples. It has been estimated that we have an illustration of the geometry dependence of the radiative energy transfer expected in crystals, since simple melting samples (about $4 \times 4 \times 3$ mm^3) had larger crystal dimensions than LHPG fibres, therefore the reabsorption probability should be much higher in simple melting crystals which promotes the radiative transfer processes. This is confirmed by cutting simple melting samples into much smaller pieces (about $1 \times 1 \times 1$ mm^3) and measuring the decay time. For example, the decay times of 30 mol% Yb^{3+}:CaF_2 samples decreased from 2.87 to 2.07 ms depending on the size of the samples.

5.3.2. Evaluation of the radiative lifetime of Yb^{3+}-doped CaF_2. The measurement of intrinsic lifetimes has received attention for a long time in the literature [27–30]. In particular, the determination of the Yb^{3+} radiative lifetime in crystals requires a lot of precaution. As an example, in YAG, measurements of the room temperature effective stimulated emission cross-section have ranged from 1.6×10^{-20} to 2.03×10^{-20} cm^2 [25, 31]. Depending on the concentration and size of samples, we have seen in the previous section that the self-trapping process is more or less involved. The gradient concentration fibre is a unique tool to make the correlation between Yb^{3+} concentration and decay time measurements which have been measured *in situ* on the same sample in relation to the distance from the top of the crystallized rod. By using a reference made of a homogeneous single crystal fibre of well-defined composition, the two curves were correlated. Because the volume of materials excited is steady, radiative trapping due to the geometrical effect can be supposed to be a constant value for each concentration, and it should be weak due to the small size of the excited sample.

The intrinsic lifetime can be read by following the concentration dependence to the lowest values in figure 8. The value has been estimated to be 2.05 ± 0.01 ms.

The direct calculation of the spontaneous emission probability from the integrated absorption intensity [32] is adapted to confirm the radiative lifetime value. The radiative lifetime can be deduced from the absorption spectrum according to the formula (2):

$$1/\tau_{rad} = A_{if} = \frac{g_f}{g_i} \frac{8\pi n^2 c}{\lambda_0^4} \int \sigma_{fi}(\lambda)\, d\lambda \qquad (2)$$

where g is the degeneracy of the initial and final states ($g_f = 4$ for $^2F_{7/2}$ and $g_i = 3$ for $^2F_{5/2}$), n is the refractive index ($n = 1.43$), c is the light velocity, λ_0 is the mean wavelength of the absorption peak (980 nm), $\sigma(\lambda)$ is the absorption cross-section at wavelength λ. The radiative lifetime was calculated as $\tau_{rad\ (theo)} = 2.0$ ms by equation (2) quite close to the experimental value of $\tau_{rad\ (exp)} = 2.05$ ms. The lower value of $\tau_{rad\ (theo)}$ with respect to $\tau_{rad\ (exp)}$ might be related to the over estimation of the value of the integrated absorption cross-section including all types of site at room temperature, and not only the highest population of the main square-antiprism sites.

5.3.3. Second regime: self-quenching process. The second regime corresponds to the usual quenching process by energy transfer to defects and other impurities in the host. In the case of Yb^{3+}-doped crystals, because of the presence of only one excited level, we cannot expect the excited state mechanism as a cross-relaxation process inside Yb^{3+} ions. Several types of quenching site, such as unexpected other rare earth ions and Yb^{3+} pairs in Yb:sesquioxides [17, 23, 24] and Yb:YAG [25], Yb^{2+} in Yb:YAG [33] and OH^- groups in tetraphosphate glasses [34], have been reported. In the case of $Ca_{1-X}Yb_XF_{2+X}$ crystals, we did not retain the possibility of OH^- groups. First of all, our samples did not have the OH^- group absorption band normally situated around the 3500 cm^{-1} region as it should be eliminated during the fluoride growth process unlike its presence in oxides. Secondly, we have investigated 0.5%, 5% and 30% crystals grown by the simple melting method before and after γ-irradiation to detect any traces of Yb^{2+}. In all the simple melting crystals, before γ-irradiation we did not get any evidence of Yb^{2+} absorption. Only after γ-irradiation with doses of 10^4 and 10^5 Gy, did Yb^{2+} centres arise [35].

Evidence of pairs. Only pair emission from two neighbour ions or cooperative emission from aggregates can occur in the visible spectrum (figure 9(b)), depending on the shortest distances between Yb^{3+} ions. In $Ca_{1-X}Yb_XF_{2+X}$ crystals the smallest Yb^{3+}–Yb^{3+} pair distance is 3.86 Å, and we consider such a small value as a primary factor in making efficient Yb^{3+}–Yb^{3+} pairs. Figure 10 shows visible emission spectra of $Ca_{1-X}Yb_XF_{2+X}$ crystals under $\lambda = 932$ nm excitation. (a) $x = 0.05$ by simple melting, (b) $x = 0.3$ by simple melting, (c) $x = 0.05$ by the LHPG method and (d) $x = 0.3$ by the LHPG method. Each crystal was measured with three different time resolutions ((i), (ii) and (iii) correspond to gate width $= 20\ \mu$s, 100 μs and 1 ms, respectively. Gate delay $= 0$ s for all measurements.) As can be seen in figure 10, green emission from pairs around 490–510 nm have been effectively detected by time resolved spectroscopy to avoid the overlapping of the strongest intensity coming from other impurities. Broken lines indicate the convolution from the infrared emission spectra as already explained in [1, 17, 36], and we can say that theoretical calculation has a good match with the experimental spectra at short times. Consequently, the presence of both pairs and aggregates of Yb^{3+} are here the signature of the assumed clusters in this crystal.

When we consider these spectra in relation to the two different growth methods, it is obvious that crystals grown by the LHPG method have a higher emission intensity of Yb^{3+} pairs
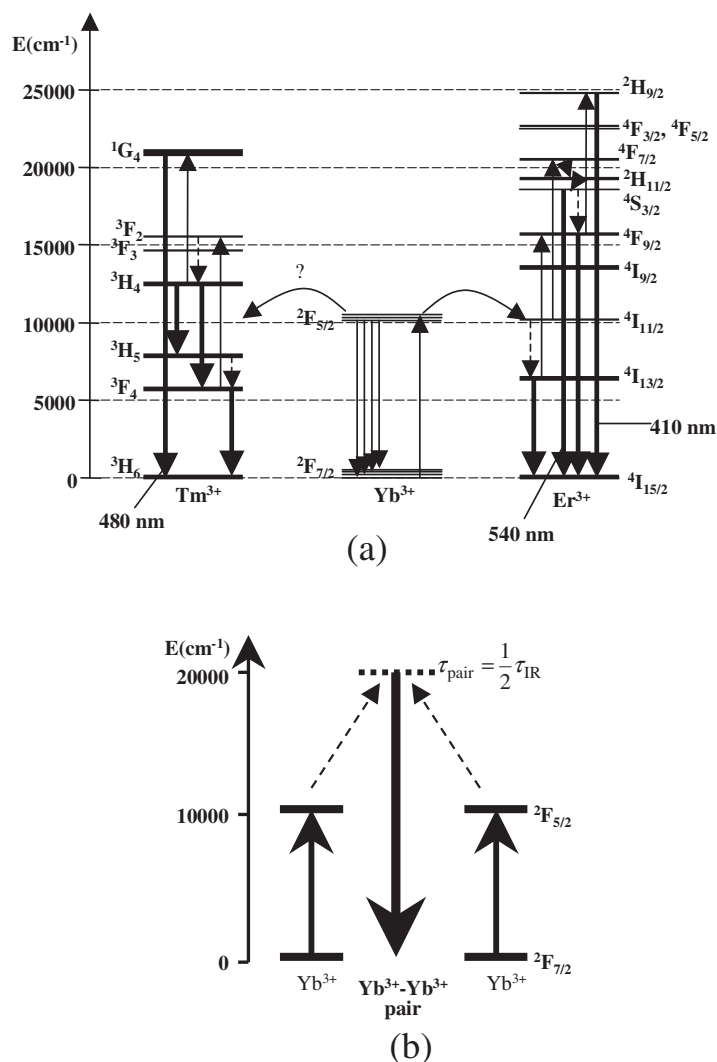
Figure 9. Energy level diagram of (a) energy transfer from Yb^{3+} to Er^{3+} and Tm^{3+} and (b) pairs of Yb^{3+}.

than that of simple melting. Fundamentally, there is no big difference in impurity concentration between the two growth methods since these crystals were prepared from the same raw materials and the solidification fraction was 1.0 in both methods. Therefore, the difference in Yb^{3+} pair intensity does not come from the ratio between impurities and Yb^{3+} pairs. The Yb^{3+} pair intensity should really be higher in the crystals using the LHPG method. This means that crystals prepared by the LHPG method have lower uniformity and then contain a lot of pairs, which is caused by a higher crystallization rate with respect to the simple melting method. Such pairs could bring a higher self-quenching effect as has been recently suggested by Auzel [37]. Therefore it could be one of the reasons why the concentration gradient fibres show shorter decay times than those of the crystals prepared by simple melting.

   This is an important feature which might be associated with an intrinsic self-generated quenching centre for lanthanide-doped high-purity solids [37]. This centre, in fact a cluster-
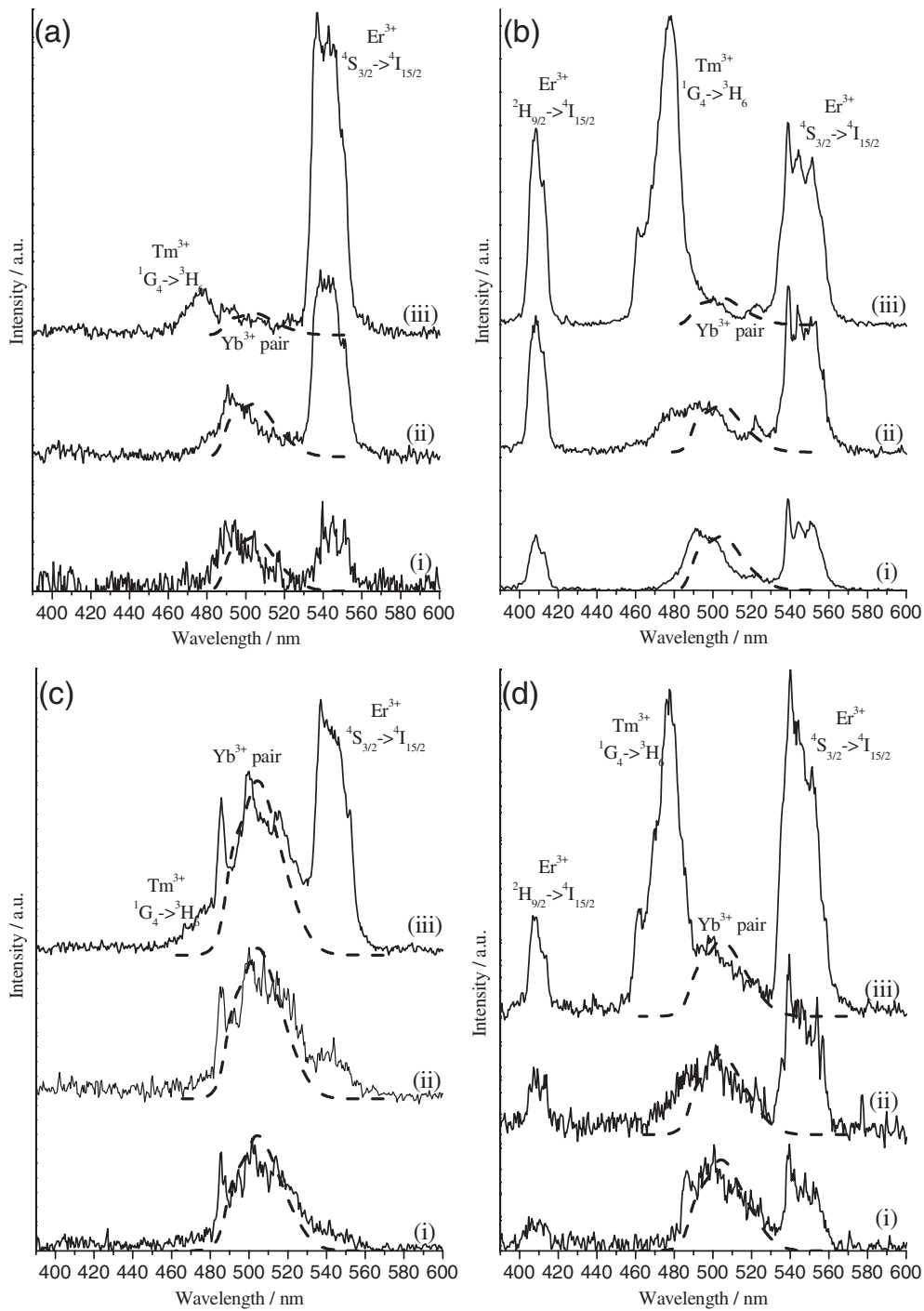
Figure 10. Emission spectra of $Ca_{1-X}Yb_XF_{2+X}$ crystals in the visible region under $\lambda = 932$ nm excitation (a) $x = 0.05$ by simple melting, (b) $x = 0.3$ by simple melting, (c) $x = 0.05$ by the LHPG method and (d) $x = 0.3$ by the LHPG method. In each figure, (i), (ii) and (iii) correspond to gate width $= 20$ μs, 100 μs and 1 ms, respectively. Gate delay $= 0$ s for all measurements. Broken curves indicate the convolution from IR emission spectra.

Table 3. Determination of impurities by high resolution glow discharge mass spectrometry (HR-GDMS) for $Ca_{0.95}Yb_{0.05}F_{2.05}$ prepared by simple melting.

Concentration (wt ppm)		
Er	Tm	Ce
0.08	0.06	<0.05

like pair of active centres, is shown to come from a particular multiphonon-assisted energy transfer between them. Being due to the vibronic properties of the host it cannot be suppressed. However, the first essays to fit the theoretical law of this process were unsuccessful in Yb^{3+}-doped sesquioxides [24] since the decrease of decay time in the high dopant concentration region has been assigned with a much higher probability to an energy transfer through Yb^{3+} excited ion to rare earth unwanted impurities.

Evidence of rare earth unexpected ions. In $Ca_{1-X}Yb_XF_{2+X}$ samples, the presence of rare earth impurities has also been observed, as can be seen in figure 10, even starting with materials with a purity of 99.99% as used in this study. Because rare earth elements are indeed chemically related, it is difficult to separate them from each other. Thus, impurities are inevitable. The presence of rare earth impurities was also proved by high resolution glow discharge mass spectrometry (HR-GDMS) analysed by *Shiva Technologies Europe* as shown in table 3. Moreover, looking at the Dieke diagram, one can see that many resonant energy transfers are possible between trivalent rare earth ions. In particular, in the $10\,000\,cm^{-1}$ energy range matching with the excited state of Yb^{3+} ions, resonant energy transfer is allowed with the $^4I_{11/2}$ excited level of Er^{3+} ions and non-resonant energy transfer is also known with Tm^{3+} ions. This process was observed as concentration quenching in almost all the Yb^{3+}-doped oxides we were analysing [23, 24]. The decreased decay time in the high dopant concentration region can be assigned to energy transfer by up-conversion (ETU, also called APTE) leading to the de-excitation of the emitting level of Er^{3+} (and Tm^{3+}) to unexpected impurities according to the model drawn in figure 9(a).

As can be seen in figure 10, the emissions around 537–555 nm are considered as the up-conversion energy transfer from the $^2F_{7/2} \rightarrow {}^2F_{5/2}Yb^{3+}$ absorption transition to the $Er^{3+}\,{}^4I_{11/2} \rightarrow {}^4F_{7/2}$ absorption transition followed by the $^4S_{3/2} \rightarrow {}^4I_{15/2}$ emission transition [38]. The $^2H_{9/2} \rightarrow {}^4I_{15/2}$ emission transition around 408 nm is also coming from an up-conversion process to Er^{3+}, most probably from two steps in Er^{3+} ions as can be observed in figure 9(a). This latter emission was observed only in higher dopant concentration samples that are $Ca_{0.85}Yb_{0.15}F_{2.15}$ and $Ca_{0.7}Yb_{0.3}F_{2.3}$. This is the proof that higher concentration doping promotes the up-conversion energy transfer processes to impurities and, as a matter of fact, self-quenching phenomena.

Figure 11 shows the decay curve forms of three different wavelengths for $Ca_{0.7}Yb_{0.3}F_{2.3}$ crystal grown by the simple melting technique, corresponding to Yb^{3+} pair (500 nm) $Er^{3+}\,{}^4S_{3/2} \rightarrow {}^4I_{15/2}$ (540 nm) and $Tm^{3+}\,{}^1G_4 \rightarrow {}^3H_6$ (480 nm) emissions. The 500 nm emission exhibits an exponential decay curve characterized by $\tau = 0.94$ ms, that is about half of the $^2F_{5/2}$ decay time as expected for Yb^{3+} pair emission [36, 39].

As the 478 nm emission shows an initial rise-time delay like the red and the green ones from Er^{3+} ions, we observe it only when we apply a long gate width. This emission is considered as the up-conversion of $Tm^{3+}\,{}^1G_4 \rightarrow {}^3H_6$ by the energy transfer from Yb^{3+} [40]. The intensity of this emission greatly changed depending on dopant concentration as the Er^{3+} 408 nm emission line. The process by which we reach so high an energy level in Tm^{3+} is not so clear. There are
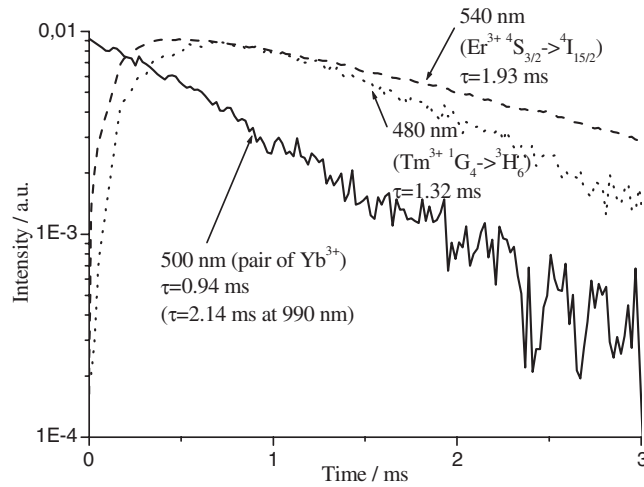
Figure 11. The decay curve forms of $Ca_{0.7}Yb_{0.3}F_{2.3}$ crystal by simple melting, corresponding to $Er^{3+} {}^4S_{3/2} \rightarrow {}^4I_{15/2}$ (540 nm), $Tm^{3+} {}^1G_4 \rightarrow {}^3H_6$ (480 nm) and pairs of Yb^{3+} (500 nm) emissions.

no resonant levels between the $Yb^{3+} {}^2F_{5/2}$ and $Tm^{3+} {}^3H_5$ electronic levels so that we have to accept ${}^3H_5$ vibronic level occurrence as observed in the avalanche photon process, or we should consider the excitation of the $Tm^{3+} {}^1G_4$ level via the up-conversion process into $Er^{3+} {}^2H_{9/2}$ and relaxation to the $Er^{3+} {}^4F_{7/2}$ level which is nearly resonant with the $Tm^{3+} {}^1G_4$ level. Another up-conversion can occur in Er^{3+} ions by the relaxation ${}^4I_{11/2} \rightarrow {}^4I_{13/2}$ to the ${}^4I_{13/2}$ metastable level which is the IR emitting level around 1.54 μm. The up-conversion process is then the ${}^4I_{13/2} \rightarrow {}^4F_{9/2}$ transition in resonance with Yb^{3+} emission, populating again the ${}^4F_{9/2}$ level giving rise to red emission, favourable again for the up-conversion to the ${}^2H_{9/2}$ higher level at the origin of the violet emission around 408 nm. This means that the elucidation of real involved energy transfer mechanisms between Yb^{3+} and traces of Er^{3+} and Tm^{3+} impurities have to be questioned to interpret such easy observation of up-conversion effects.

Model of quenching processes. A recent model [24] has been submitted to interpret concentration quenching processes and applied in Yb:sesquioxides. The self-trapping process has been treated by the Milne approach used for radiation trapping in a gas medium [41] with 'weak opacity'. It is based on a Compton type spatial diffusion equation containing the Einstein relationships between spontaneous and induced emission and absorption but neglecting the population inversion. In the case of 'weak opacity' the previous hypotheses leads to:

$$\tau_t = \tau_i(1 + \sigma Nl) \tag{3}$$

where τ_t is the measured lifetime in the trapping conditions, τ_i is the intrinsic lifetime without trapping, σ is the transition cross-section, N is the ion doping concentration, and l is the average absorption length in the lifetime measurement experiment.

The theoretical aspects showed that self-quenching behaviour, for a rather large doping range, cannot be explained by fast diffusion towards intrinsic non-radiative centres but well described by a limited diffusion process within the doping ion subsystem towards impurities analogous to the doping ions themselves. When the quenching centre is an impurity analogous to the active centre and having levels in resonance or quasi resonance with the considered ion first excited state, the quenching probability can be of the same order as the transfer probability

for diffusion within the considered ion subsystem. In such a case, assuming an electric dipole–dipole interaction, the self-quenching behaviour can be simply described as equation (4):

$$\tau(N) = \tau_{\text{rad}}/[1 + (9/2\pi)(N/N_0)^2] = \tau_{\text{w}}/[1 + (9/2\pi)(N/N_0)^2] \tag{4}$$

where τ_{w} is the measured lifetime at weak concentration which can be adopted as the radiative lifetime. Consequently, $\tau(N)$ is indeed the multiplication of the two main processes as equation (5):

$$\tau(N) = \frac{\tau_{\text{w}}(1 + \sigma Nl)}{1 + (9/2\pi)(N/N_0)^2}. \tag{5}$$

Here, N is the concentration of active ions, $\tau(N)$ is the ions excited state lifetime at the concentration N, N_0 is the critical concentration, σ is the transition cross-section and l is the average absorption length in the lifetime measurement experiment.

The theoretical fittings are shown in figure 8, as a broken curve for the simple melting growth and as a continuous curve for the LHPG method. The fitting parameters of both simple melting and LHPG methods were found to be $\tau_{\text{w}} = 2.05$ ms close to the theoretical value of the radiative lifetime of 2.0 ms, $\sigma l = 2.9 \times 10^{-22}$ cm^3 (0.071 cm^3/%), $N_0 = 7.47 \times 10^{21}$ cm^{-3} (32%) for simple melting samples and $\sigma l = 1.7 \times 10^{-22}$ cm^3 (0.041 cm^3/%), $N_0 = 7.47 \times 10^{21}$ cm^{-3} (32%) for the LHPG samples.

N_0 is the parameter of self-quenching, hence much higher N_0 values than that of Yb:Y$_2$O$_3$ ($N_0 = 1.9 \times 10^{21}$ cm^{-3}) and Yb:YAG ($N_0 = 2.3 \times 10^{21}$ cm^{-3}) [42] mean weaker self-quenching probability as compared with oxide laser crystals. Such weak self-quenching probability is an agreeable property in laser applications. It is also interesting that the two curves showed the same N_0 value. This means that the two curves have theoretically the same self-quenching probability, which confirms that the difference in decay time dependence between the two growth methods mainly comes from the self-trapping process and not from the self-quenching processes.

Finally, it is shown that self-quenching, for a rather large doping range, is well described by a limited diffusion process within the doping ion subsystem towards impurities analogous to the doping ions themselves.

5.4. Theoretical approach of the laser material optimization

From the results of fittings in the previous section, it is now possible to obtain the experimental points corrected for trapping by simply deconvoluting the experimental values by the trapping function (3) with the σl values. The corrected experimental points are shown in figure 12. On the other hand, by using the fitting parameters, τ_{w} and N_0, the self-quenching curve simulation as given by equation (4) could also be obtained as the broken curve in figure 12. As can be seen, the 'real' self-quenching curve obtained by equation (4) is corresponds well with the corrected experimental points.

Now, with the help of this continuous reliable mathematical curve for self-quenching, it is possible to determine in a simple and unambiguous way the material optimum concentration for its active optical use [24]. From the steady state rate equation, the material gain is simply given by:

$$G = \exp[\sigma_{\text{g}}\sigma_{\text{a}}N\tau(N)l] \tag{6}$$

where σ_{g} is the gain cross-section taking care of the quasi three-level situation for a laser between first excited and ground state, σ_{a} is the pump absorption cross-section for the pumping wavelength, N is the chemical concentration of active ions, $\tau(N)$ is the ions' excited state lifetime at the considered concentration N and l is the amplification length.
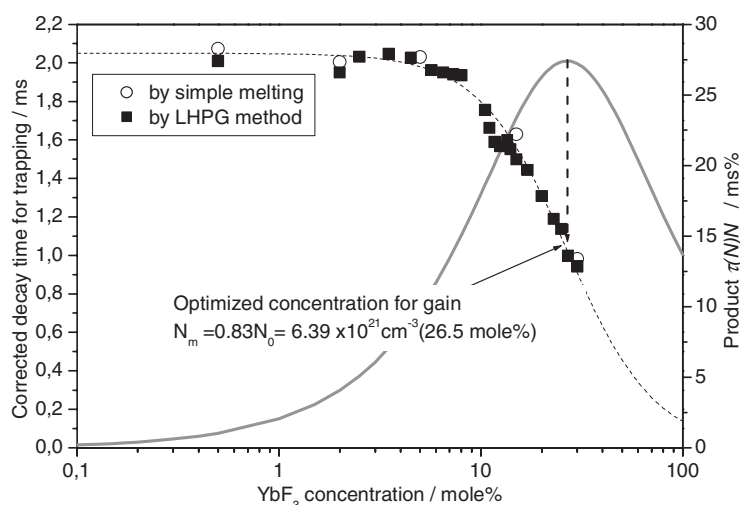
Figure 12. Experimental decay times with correction for the self-trapping effect according to equation (3). The broken curve indicates the theoretical curve for the limited diffusion case according to equation (4). The continuous curve indicates the optimization of the optical gain by the product $\tau(N)N$.

From equation (4), the product $\tau(N)N$, can be optimized easily. It is plotted in figure 12 as a continuous curve. It is shown that the maximum value, namely the optimum Yb^{3+} concentration for gain, N_m, in CaF_2 is 6.39×10^{21} cm^{-3} (26.5 mol%). Since this maximum value is unique, it has been proposed to consider such a value in cm^{-3} as an absolute scale for self-quenching characterizing any given host-doping couple and applied to $Yb^{3+}:Y_2O_3$ in which the optimum concentrations for gain, N_m, has been found to be 1.6×10^{21} cm^{-3} (6%) [24]. However, concentration of the impurities should be also considered since it is an essential factor for self-quenching behaviour. Here, we remark again that the purity of raw materials was 99.99% and rare earth impurities in 5% $Yb^{3+}:CaF_2$ crystals prepared by simple melting were found to be 0.05–0.08 wt ppm.

As the N_m was found to be equal to $0.83N_0$, then the critical concentration itself, which from equation (4) can be simply defined as the concentration reducing τ_w to $0.50\tau_w$ (1.02 ms) is a good indication of the self-quenching magnitude and can also easily provide the optimum concentration.

Very recent results obtained on the laser emission of Yb^{3+}-doped CaF_2 between 1000 and 1060 nm, presented in COLOQ 8, confirm both the potentiality and the tuneable range of the infrared laser emission [43]. Measurements on our samples are in progress and will be compared both with the results of [43] and with those which would be obtained in other Yb^{3+}-doped crystals which are grown either at the UCBLyon1 or at the Tohoku University in Japan.

6. Summary

$Ca_{1-X}Yb_XF_{2+X}$ crystals were prepared by the simple melting method under CF_4 atmosphere and by the LHPG method under Ar atmosphere. Consequently, we were able to compare spectroscopic properties depending on the growth conditions, and the ingots from the simple melting were used as raw materials for the growth of crystalline fibres by the LHPG method.

Concentration gradient $Ca_{1-X}Yb_XF_{2+X}$ fibres with diameter of 1.0 mm were successfully grown by the LHPG method.

Absorption and emission spectra at room temperature and 12 K showed several crystallographic sites associated with Yb^{3+} electronic transitions between Stark levels and their vibronic peaks due to a strong electron–phonon coupling. We have assigned, above 0.5 mol% Yb^{3+}, the occupied different crystallographic sites to the average square-antiprism sites, indeed the set of square-antiprisms in several cuboctahedral-related anion clusters, the tetragonal and the trigonal sites at low concentration and the T_2 (O^{2-}) perturbed site which is mainly observed in the LHPG samples.

Experimental decay time dependence on dopant concentration was studied using concentration gradient fibres. This suggests typically competitive phenomena between two processes: the increasing of decay time due to radiative energy transfer (self-trapping) and the decreasing of decay time due to self-quenching which is connected to non-radiative energy transfer from Yb^{3+} ions to unexpected Er^{3+} and Tm^{3+} rare earth ions in the host for a rather large doping range, which is well described by a limited diffusion process within the doping ion subsystem towards impurities. A model has been used to fit the decay time measurements. Important parameters found for laser application are the Yb^{3+} radiative lifetime close to 2.05 ms, the critical concentration $N_0 = 7.47 \times 10^{21}$ cm^{-3} (32 mol%) and the optimum concentration for gain $N_m = 6.39 \times 10^{21}$ cm^{-3} (26.5 mol%). Large N_0 and N_m values, several times bigger than oxides, are agreeable properties for laser application as tuneable solid-state lasers and luminescent applications in general. Energy transfer to unwanted Er^{3+} and Tm^{3+} impurities have been observed by the up-conversion mechanism under IR Yb^{3+} pumping, confirming the main contribution in the quenching mechanism. In addition, Yb^{3+} pairs have been pointed out and investigated with a possible occurrence in the quenching mechanism.

Acknowledgments

References

[1] Boulon G, Brenier A, Laversenne L, Guyot Y, Goutaudier C, Cohen-Adad M T, Métrat G and Muhlstein N 2002 *J. Alloys Compounds* **341** 2
[2] Brenier A and Boulon G 2002 *J. Alloys Compounds* **323/324** 210
    Brenier A and Boulon G 2001 *Europhys. Lett.* **55** 647
[3] Bourdet G L 2001 *Opt. Commun.* **198** 411
[4] Sobolev B P and Fedorov P P 1978 *J. Less-Common Met.* **60** 33
[5] Campbell J A, Laval J-P, Fernandez-Diaz M-T and Foster M 2001 *J. Alloys Compounds* **323/324** 111
[6] Grigor'eva N B, Otroshchenko L P, Maksimov B A, Verin I A, Sobolev B P and Simonov V I 1996 *Crystallogr. Rep.* **41** 607
[7] Lavel J P, Abaouz A, Frit B and Lebail A 1990 *J. Solid State Chem.* **85** 133
[8] Lavel J P, Abaouz A and Frit B 1989 *J. Solid State Chem.* **81** 271
[9] Ness S E, Bevan D J M and Rossell H J 1988 *Eur. J. Solid State Inorg. Chem.* **25** 509
[10] Bevan D J M, McCall M J, Ness S E and Taylor Max R 1988 *Eur. J. Solid State Inorg. Chem.* **25** 517
[11] Bouffard M, Jouart J P and Joubert M-F 2000 *Opt. Mater.* **14** 73
[12] Kirton J and McLaughlan S D 1967 *Phys. Rev.* **155** 279
[13] Kirton J and White A M 1969 *Phys. Rev.* **178** 543

[14] Ayala A P, Oliveira M A S, Gesland J-Y and Moreira R L 1998 *J. Phys.: Condens. Matter* **10** 5161
[15] Burns J H, Ellison R D and Levy H A 1968 *Acta Crystallogr.* B **24** 230
[16] Laversenne L, Kairouani S, Guyot Y, Goutaudier C, Boulon G and Cohen-Adad M Th 2002 *Opt. Mater.* **19** 59
[17] Boulon G, Laversenne L, Goutaudier C, Guyot Y and Cohen-Adad M T 2003 *J. Lumin.* **102/103** 417
[18] DeLoach L D, Payne S A, Chase L L, Smith L K, Kway W L and Krupke W F 1993 *IEEE J. Quantum Electron.* **29** 1179
[19] Bensalah A, Guyot Y, Ito M, Brenier A, Sato H, Fukuda T and Boulon G 2003 *Opt. Mater.* at press
[20] Voron'ko Yu K, Osiko V V and Shcherbakov I A 1969 *Sov. Phys.—JETP* **29** 86
[21] Falin M L, Gerasimov K I, Latypov V A, Leushin A M, Bill H and Lovy D 2003 *J. Lumin.* **102/103** 239
[22] Buchanan R A, Wickersheim K A, Pearson J J and Herrmann G F 1967 *Phys. Rev.* **159** 245
[23] Laversenne L, Goutaudier C, Guyot Y, Cohen-Adad M Th and Boulon G 2002 *J. Alloys Compounds* **341** 214
[24] Auzel F, Baldacchini G, Laversenne L and Boulon G 2003 *Opt. Mater.* **24** 103
[25] Yoshikawa A, Boulon G, Laversenne L, Canibano H, Lebbou K, Collombet A, Guyot Y and Fukuda T 2003 *J. Appl. Phys.* **94** 5479
[26] Haumesser P-H, Gaume R, Viana B, Antic-Fidancev E and Vivien D 2001 *J. Phys.: Condens. Matter* **13** 5427
[27] Sumita D S and Fan T Y 1994 *Opt. Lett.* **19** 1343–5
[28] Uehara N, Ueda K and Kubota Y 1996 *Japan. J. Appl. Phys.* **35** L499
[29] Hehlen M P 1996 *OSA TOPS on Advanced Solid-State Lasers* vol 1, ed S A Payne and C Pollock, p 530
[30] Christensen H P, Gabbe D R and Jenssen H P 1982 *Phys. Rev.* B **25** 1467
[31] Bruesselbach H W, Sumida D S, Reeder R A and Byren R W 1997 *IEEE J. Sel. Top. Quantum Electron.* **3** 105
[32] Weber M J 1971 *Phys. Rev. B* **4** 3153
[33] Yang P, Deng P and Yin Z 2002 *J. Lumin.* **97** 51
[34] Zhang L and Hu H 2002 *J. Phys. Chem. Solids* **63** 575
[35] Kaczmarek S, Tsuboi T, Ito M and Boulon G 2003 *Euro. Phys. J. Appl. Phys.* submitted
[36] Guyot Y, Moncorgé R, Merkle L D, Pinto A, McIntosh B and Verdun H 1996 *Opt. Mater.* **5** 127
[37] Auzel F 2002 *J. Lumin.* **100** 125
[38] Cheng Z X, Zhang S J, Song F, Guo H C, Han J R and Chen H C 2002 *J. Phys. Chem. Solids* **63** 2011
[39] Nakazawa E and Shionoya S 1970 *Phys. Rev. Lett.* **25** 1710
[40] Demidovich A A, Kuzmin A N, Nikeenko N K, Titov A N, Mond M and Kueck S 2002 *J. Alloys Compounds* **341** 124
[41] Milne E A 1926 *J. Lond. Math. Soc.* **1** 1
[42] Goutaudier C, Lebbou K, Guyot Y, Ito M, Cañibano H, El Hassouni A, Laversenne L, Cohen-Adad M T and Boulon G 2003 *Ann. Chim., Sci. Mater.* **28** 78
[43] Camy P, Doualan J L, Petit V, Renard S and Moncorgé R 2003 *COLOQ8: Proc. '8ème Colloque sur les Lasers et l'Optique Quantique' (Toulouse, France, Sept. 2003)*